Available online at www.sciencedirect.com
ScienceDirect
Trans. Nonferrous Met. Soc. China 31(2021) 3785−3799
Transactions of Nonferrous Metals Society of China
www.tnmsc.cn

Heterogeneous structure-induced strength and ductility synergy of α-brass subjected to rapid cooling friction stir welding

Nan XU, Lei CHEN, Bo-kun GU, Zi-ke REN, Qi-ning SONG, Ye-feng BAO

College of Mechanical and Electrical Engineering, Hohai University, Changzhou 213022, China

Received 17 January 2021; accepted 23 July 2021

Abstract: The 2 mm-thick α-brass plates were successfully joined using conventional friction stir welding (CFSW) with air cooling and rapid cooling friction stir welding (RCFSW) with liquid CO_2 cooling. The microstructure and mechanical properties of the two welds were carefully investigated by electron back-scattered diffraction and transmission electron microscopy. The stir zone of CFSW exhibited homogeneous equiaxed grains, while the stir zone of RCFSW showed a heterogeneous grain structure, i.e. ultrafine grains containing massive dislocations and nano twins. Compared with the CFSW, yield strength and ultimate tensile strength of RCFSW were increased by 31% and 24%, respectively. The enhanced yield strength and improved strain hardening capacity were attributed to grain boundary strengthening and dislocation strengthening. Furthermore, good ductility was achieved due to the released stress concentration of the nano twins caused by the plastic deformation.

Key words: friction stir welding; brass; microstructure; recrystallization; mechanical properties

1 Introduction

α-brass (Cu−30Zn alloy) has several advantages, such as excellent thermal conductivity, corrosion resistance, and a combination of strength and ductility. Therefore, it is typically used to manufacture containers and heat exchangers that contact corrosive media [1,2]. Welding technology is an efficient method for α-brass structure component manufacturing. In traditional fusion welding processes, large heat input is required to compensate for the heat loss resulting from the good thermal conductivity of α-brass. Therefore, defects such as cracks, porosities, and oxide inclusions usually appear in the weld. The large heat input also causes a wide heat-affected zone and a grain-coarsened fusion zone, both of which significantly reduce the tensile properties of the joint [3].

Friction stir welding (FSW) is a solid-state joining technique invented by The Welding Institute of the U.K. in 1991 [4,5]. During FSW, the processing temperature is lower than that of the melting point of the material, so defects, such as cracks and porosities, can be completely avoided [6,7]. MERAN [8] initially conducted FSW technology on α-brass in 2006. It was found that the evaporation of Zn disappeared due to the significantly reduced welding temperature as compared with that of fusion welding methods. MOGHADDAM et al [9] reported that “stir bands” usually appeared in the FSW α-brass joint owing to the formation of Cu or Zn oxides. The formation of “stir bands” decreased the strength and ductility of the stir zone (SZ). After that, SUN and FUJII [10] found that by increasing the axial pressure, the strength of the SZ significantly increased due to the enhanced dislocation density. Early FSW of α-brass was conducted under large heat input. Although the

Corresponding author: Nan XU, Tel/Fax: +86-519-85192039, E-mail: xunan@hhu.edu.cn, xunan20032389@126.com
DOI: 10.1016/S1003-6326(21)65764-3

strength of the SZ was close to or even exceeded that of the base material (BM) by optimizing the welding parameters (i.e., increasing the welding speed, decreasing the tool rotation rate, or increasing the axial pressure), the wide coarse-grained heat-affected zone reduced the welding efficiency. In recent years, rapid cooling FSW (RCFSW) has been developed to modify the microstructural features and tensile properties of α-brass joints [11]. During RCFSW, a strong cooling medium, such as liquid N_2 or liquid CO_2, is used to increase the cooling rate and reduce the peak temperature of the joint. This technology causes heat-affected zones to disappear and ultrafine grains with massive dislocations to form in the SZ. The transverse tensile test shows that the fracture occurs in the BM, indicating that the strength of the welded joint is improved. The SZ also shows a good combination of strength and ductility, i.e., the strength of the SZ increases without a significant decrease in ductility. The strength and ductility of the SZ are closely related to the microstructural characteristics, so it is important to study the strain hardening behavior during tensile deformation. Previous studies have investigated the strain hardening behavior of the SZ of various FSW metals and alloys, such as pure Cu, Mg alloy, and steel [12−14]. The strain hardening behavior of the SZ is mainly influenced by the grain size. During conventional FSW (CFSW), the slow cooling rate and high peak temperature reduce the ratio of substructures. In fact, substructures such as dislocations and deformation twins show major influence on the mechanical properties of the welded joint. However, the effect of substructures on the strain hardening behavior is generally neglected. Therefore, in this work, both CFSW and RCFSW were conducted on α-brass to produce two SZs with different microstructural characters. Electron backscatter diffraction (EBSD) and transmission electron microscopy (TEM) were used to investigate microstructural evolution. The connection between the microstructural features and tensile properties of the SZ was discussed in detail.

2 Experimental

Cold-rolled commercial α-brass plates were used as the BM in this study. The dimensions of the BM were 200 mm (length) × 100 mm (width) × 2 mm (thickness). Initially, the BM was annealed at 600 °C for 1 h to homogenize the microstructure. The chemical composition and mechanical properties of the annealed BM are given in Table 1. Before welding, the butt surfaces were cleaned with acetone and ethanol. The workpieces were tightly fixed on a steel-made backplate and then joined by CFSW and RCFSW, respectively. The FSW tool was made of WC−Co based steel. The tool had a concave shoulder (12 mm in diameter) and a columnar pin (4 mm in diameter and 1.9 mm in height). The welding parameters of CFSW and RCFSW remained constant, with a welding speed of 200 mm/min, rotation rate of 600 r/min, tilt angle of 3°, and axial pressure of 0.8 t. During the RCFSW, a liquid CO_2 nozzle with the same speed as the welding nozzle was set 50 mm behind the tool (Fig. 1).

After welding, the cross-section specimens were cut perpendicularly to the welding direction for microstructure characterizations. The specimens were mechanically ground, polished, and then etched using a mixture solution of 5 g ferric chloride, 3 mL hydrochloric acid, and 50 mL ethanol for optical microscopy (OM, Axio Imager A2m, ZEISS, Germany). EBSD was used to characterize the microstructure of the BM, the SZ, and the vicinity of the keyhole. The EBSD crystallographic data acquisition system (EDAX TSL OIM™, USA) was installed in a field-emission scanning electron microscope (SEM, JSM−7500, JEOL Ltd., Japan). EBSD examinations were conducted with an accelerating voltage of 20 keV and a step size of 0.4 μm. EBSD specimens were mechanically ground and then electropolished using a mixture solution of 250 mL phosphoric acid (Yasheng Ltd., China), 250 mL ethanol (Yasheng Ltd., China), and 500 mL distilled water. Some

Table 1 Chemical compositions and tensile properties of as-received α-brass

Chemical composition/wt.%				Tensile properties		
Cu	Zn	Fe	Pb	Ultimate tensile strength (UTS)/MPa	Yield strength (YS)/MPa	Total elongation (TE)/%
69.5	Bal.	0.05	0.03	360	115	60

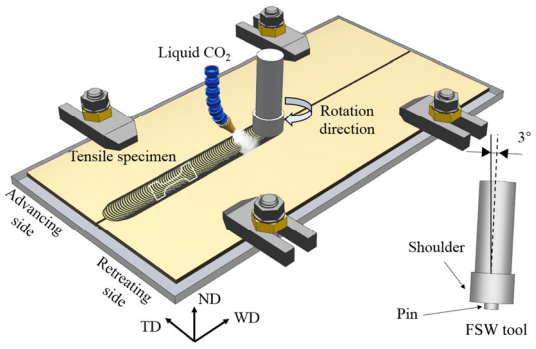

Fig. 1 Schematic diagram of RCFSW process and welding tool (The transverse direction, welding direction, and normal direction are indicated by TD, WD and ND, respectively)

liquid N_2 was added to the solution to maintain the temperature below −30 °C. The polishing voltage and time were set to be 20 V and 60 s, respectively. The average confidence index of each scan ranged from 0.57 to 0.79, and data points with a confidence index less than 0.1 were excluded. The cut-off angle was 2° when the misorientation angle was evaluated in the EBSD data. TEM (JEM−2100, JEOL Ltd., Japan) was also used to characterize the substructures of the SZ, the thermo-mechanically affected zone (TMAZ), and the vicinity of the keyhole. The accelerating voltage of the TEM examinations was 200 keV. The TEM specimens were initially ground to ~50 μm, and then further thinned using a double jet electropolishing device at 10 V and −30 °C. To investigate the tensile properties of the SZ, dog-bone shaped tensile specimens were prepared according to the standard of GB/T 2651—2008. The gauge sizes of the tensile specimen were 12 mm (length) × 4 mm (width) × 1.5 mm (thickness). Tensile tests were carried out on an Instron 3369 electronic universal material testing machine with a strain rate of 1×10^{-3} s^{-1}.

3 Results and discussion

3.1 Surface appearance

Figure 2 shows the surface appearance of the two welds. Compared with CFSW, the RCFSW joint had a bright surface and flash did not appear on the SZ side. Since the liquid CO_2 cooling decreased the peak temperature, the flowability of the materials was also reduced. The amount of material involved in the plastic flow was reduced, and no redundant materials were spilled from the edge of the shoulder. Furthermore, the cooling rate significantly increased, and no oxidation was generated on the welded surface, resulting in a bright and smooth surface appearance.

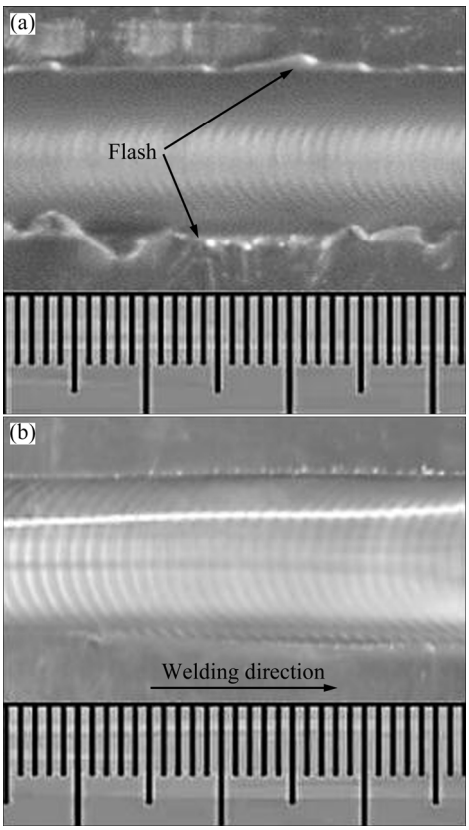

Fig. 2 Surface appearance of FSW welds: (a) CFSW; (b) RCFSW

3.2 Microstructure evolution

The OM images of the BM and SZ center are shown in Fig. 3. As a result of the annealing treatment, the BM exhibited coarse equiaxial grains with massive annealing twins. The grain structure of the two SZs was significantly refined compared with that of the BM. Specifically, the SZ of RCFSW had an ultrafine grain structure. Although the same welding parameters were adopted in the two welding processes, the grain structures in the two SZs were quite different. Liquid CO_2 sprayed from the nozzle rapidly transformed into dry ice powder and was uniformly applied to the FSW tool and the weld surface. The sublimation of the dry ice needed a large amount of heat, resulting in reduced peak temperature and enhanced cooling rate. The cooling of liquid CO_2 weakened the driving force of grain growth, resulting in an ultrafine grain structure of the SZ of the RCFSW.

Figures 4 and 5 show the EBSD results of the BM and the SZ center. The average grain size of the BM was calculated with the linear intercept method to be 36 μm. The number fraction of high-angle grain boundaries (HAGBs) was 97%, of which 58% were twin boundaries (TBs). This means that the BM showed complete annealing microstructural features. The SZ of CFSW exhibited an equiaxed grain structure with an average grain size of 9 μm. The HAGBs ratio was 85%, and 29% of them were TBs. In contrast, the SZ of RCFSW exhibited finer grains than that of CFSW, and its average grain size was shown to be 1.2 μm. The low-angle grain boundaries (LAGBs) ratio increased to 29%, and the TBs ratio decreased to 16%. Although the welding parameters were the same, the SZs exhibited different microstructures because they experienced different thermal cycles resulting from different cooling media. Cooling with liquid CO_2 had the following effects on the microstructure: (1) During severe plastic deformation (stirring stage), a lower deformation temperature led to smaller recrystallized grain sizes; (2) During the post-welding stage, the increased cooling rate inhibited grain growth, leading to a reduced ratio of TBs; (3) Enhanced cooling rate hindered the recovery and annihilation of dislocations, resulting in an increased LAGBs ratio.

Figure 6 shows the microtexture of the SZ center. During FSW, the materials experienced severe shear deformation due to the high-speed rotating tool, causing shear textures to be formed in

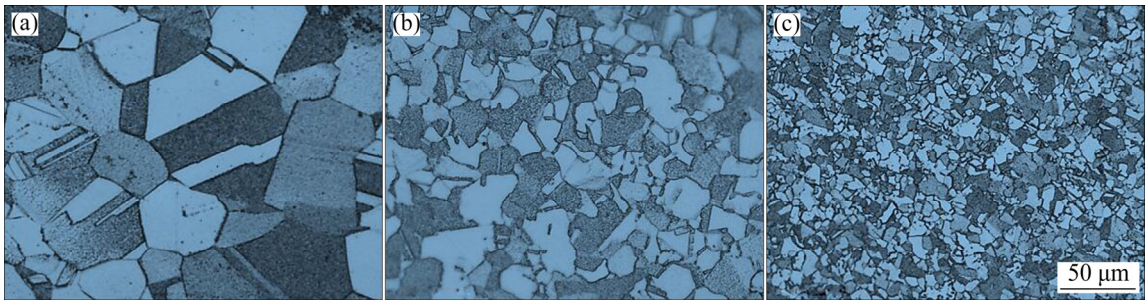

Fig. 3 OM microstructures: (a) BM of CFSW; (b) SZ of CFSW; (c) SZ of RCFSW

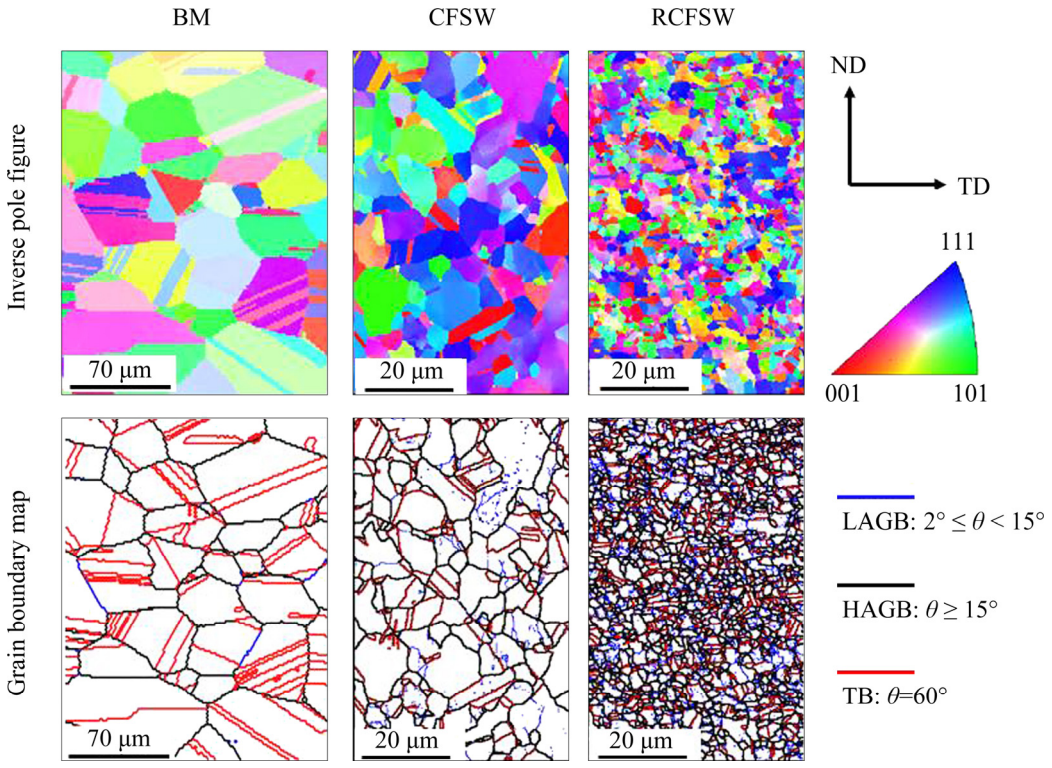

Fig. 4 EBSD characterization results of BM and SZs

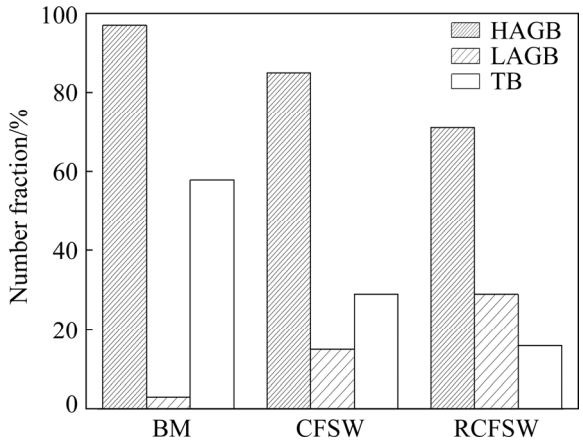

Fig. 5 Histogram of misorientation angle distribution of BM and SZs

the SZ. The shear texture is usually described in term of $\{hkl\}\langle uvw\rangle$, in which the $\{hkl\}$ plane and the $\langle uvw\rangle$ direction are parallel to the shear plane (pin surface) and shear direction (the tangent direction of the pin surface), respectively [15]. The SZ of the RCFSW showed a B-type $\{112\}\langle 110\rangle$ shear texture. This texture is usually formed in face-centered cubic (FCC) metals or alloys that are subjected to shear deformation [14], indicating that the materials receive simple shear deformation during the FSW. However, the SZ obtained by CFSW showed the textures containing B-type $\{112\}\langle 110\rangle$ and Goss-type $\{110\}\langle 001\rangle$ components, and the strength of the B-type $\{112\}\langle 110\rangle$ component was significantly weakened. The Goss-type $\{110\}\langle 001\rangle$ texture is usually considered as recrystallization texture in deformed FCC metals or alloys [15]. This means that recrystallization or grain growth occurring in the SZ of CFSW was caused by the post-annealing effect. As it was difficult to produce dislocations during grain deformation with Goss-type $\{110\}\langle 001\rangle$ orientation, the sample showed a relatively low dislocation density in the grains interior. During the air cooling stage, selective grain growth occurred in SZ, i.e., the grains with Goss-type $\{110\}\langle 001\rangle$ orientation grew preferentially [16]. Therefore, the texture intensity of the Goss-type $\{110\}\langle 001\rangle$ orientation was enhanced, while the texture intensity of the B-type $\{112\}\langle 110\rangle$ orientation was weakened.

During CFSW, the post-annealing effect can cause dislocation recovery and selective grain growth, which affect the accuracy of the analysis of microstructure evolution during welding. Therefore, an RCFSW joint was selected as a research target to discuss the grain refinement mechanism during the FSW process. The OM image of the transition zone of the RCFSW joint is shown in Fig. 7(a). The

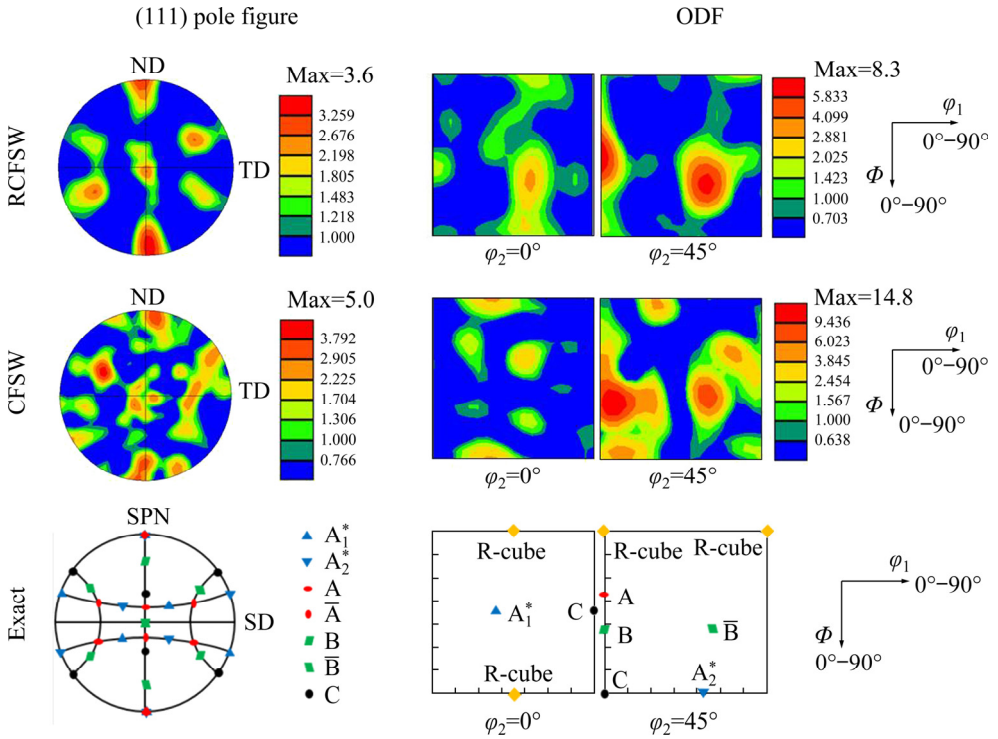

Fig. 6 Experimental and exact microtexture results including (111) pole figures and orientation distribution function (ODF) maps of SZs obtained by CFSW and RCFSW

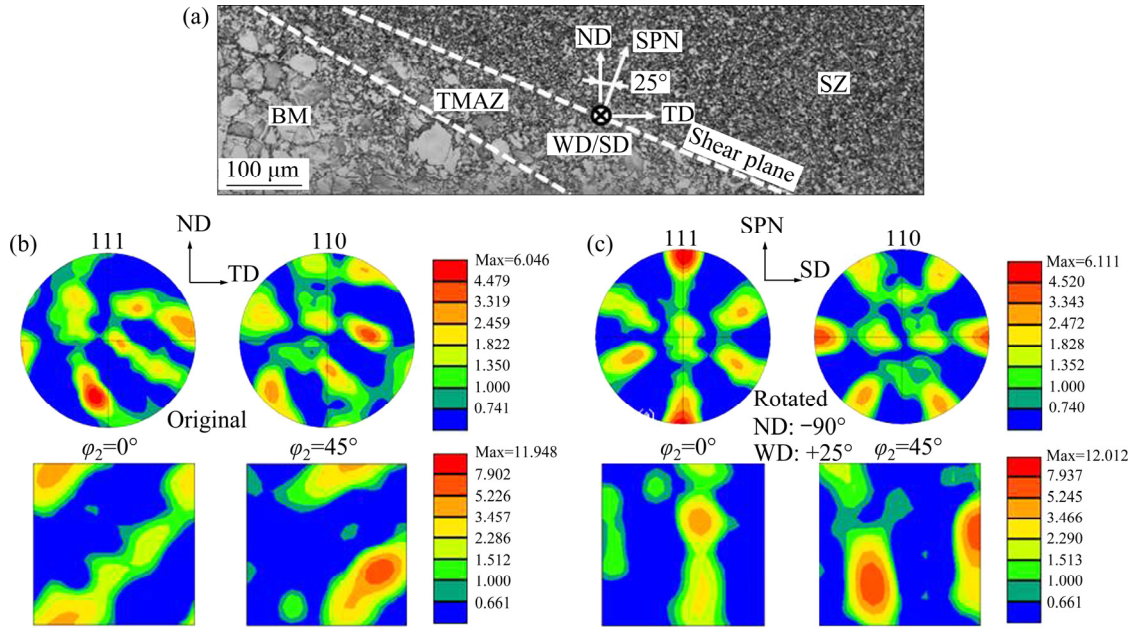

Fig. 7 OM image of transition zone of RC-FSW joint (a), original pole figures and ODF maps (b) and rotated pole figures and ODF maps (c)

thermo-mechanically affected zone (TMAZ), which is a transition region between the BM and the SZ, is of significant importance to learn the grain refinement mechanism during FSW. The TMAZ showed an extremely inhomogeneous grain structure, indicating that the partial dynamic recrystallization (DRX) occurred in this region. Figure 7(b) shows the original (111) and (110) pole figures and orientation distribution function (ODF) maps of the TMAZ. Compared with the exact (111) pole figures and ODF maps (shown in Fig. 6), these figures deviated from the exact position. Since the shear plane normal (SPN) and shear direction (SD) are not parallel to the ND and TD in the TMAZ, the FSW shear plane can be approximately described as a conical surface parallel to the boundary between the TMAZ and the SZ [17]. As a result, the SPN and the SD vary with changes in material positions. Therefore, when analyzing the texture of the TMAZ, it is necessary to rotate the original pole figures to ensure SPN and SD consistency with the exact pole figures. Figure 7(c) shows the rotated pole figures and ODF maps. It can be seen that the TMAZ also exhibits a B-type {112}⟨110⟩ orientation, indicating that the TMAZ experienced a shear deformation process similar to the SZ.

Previous studies have reported that the grain refinement during the FSW of FCC metals or alloys is attributed to dynamic recrystallization (DRX). Continuous DRX is the main recrystallization mechanism for FCC metals or alloys with high stacking fault energy (SFE), while discontinuous DRX is dominant for materials with middle/low SFE [18]. Figures 8 and 9 show the EBSD results and TEM images of the TMAZ in the RCFSW joint. As shown in Figs. 8(e) and 9(a), a new grain was formed at the bulged original grain boundary. The bulging phenomenon is related to the strain-induced grain boundary migration, which indicates that discontinuous DRX has occurred [19]. As shown in Fig. 8(b), several HAGB fragments were observed instead of the continuous LAGBs, indicating that LAGBs were transformed into HAGBs (Fig. 9(b)). This is a typical microstructural feature of continuous DRX. Continuous DRX grains are formed by the rotation of subgrains, which is different from discontinuous DRX [20]. TBs also play an important role in the grain refinement [21]. As shown in Figs. 8(c) and 9(c, d), the straight annealing TB was transformed into a serrated boundary, and its thickness decreased due to continuous plastic deformation. Then, the adjacent TBs connected, resulting in the formation of fine recrystallization grains. This indicates that the geometric DRX occurred during welding [22]. Figure 8(d) shows that the original

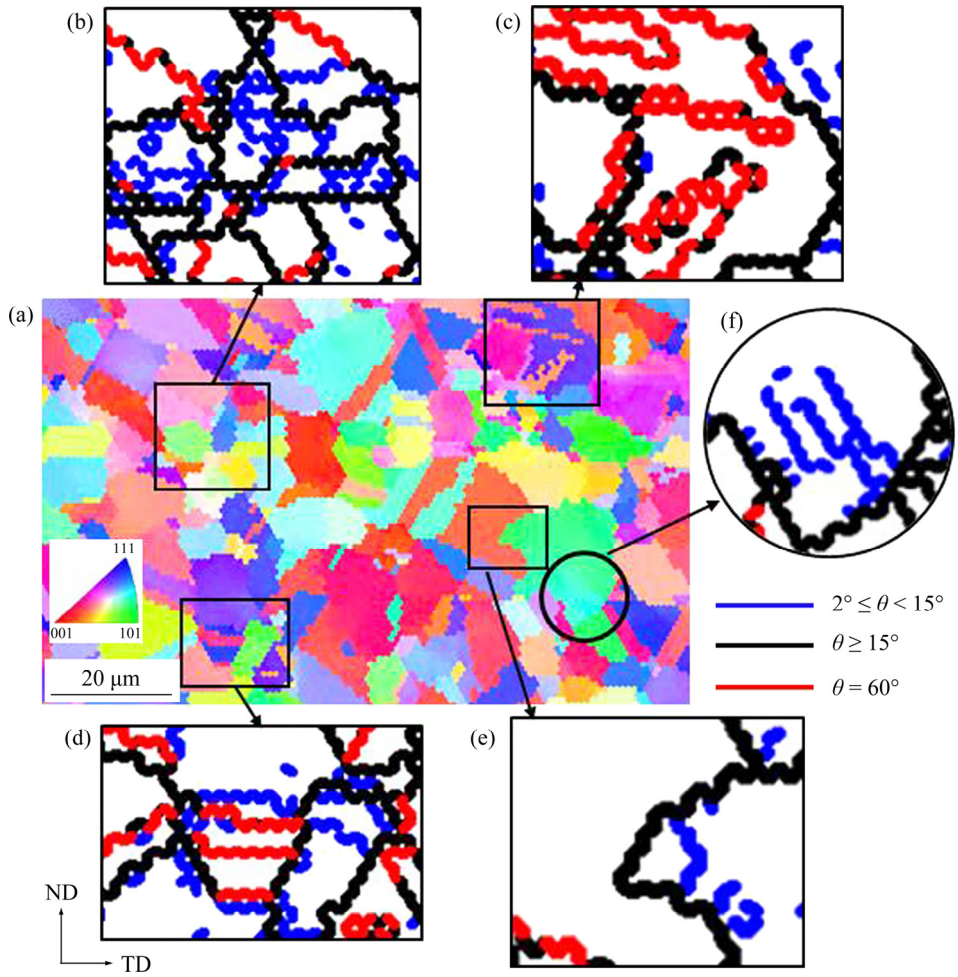

Fig. 8 EBSD results of TMAZ in RCFSW joints: (a) Inverse pole figure; (b−f) Selected enlarged regions shown as grain boundary maps

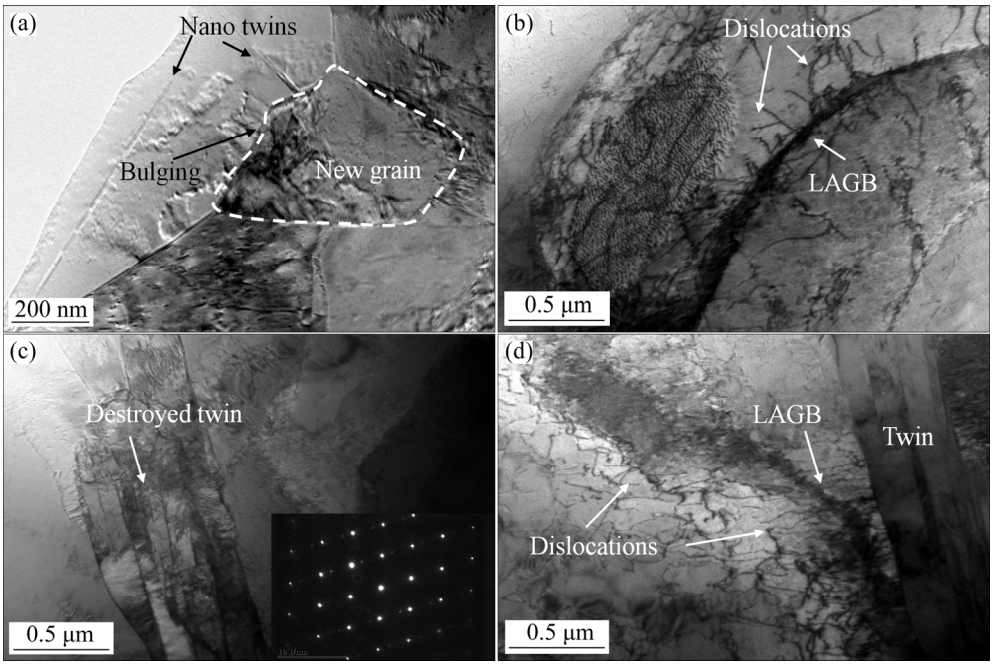

Fig. 9 TEM images of TMAZ in RCFSW joint, showing different grain refinement mechanisms: (a) Discontinuous DRX; (b) Continuous DRX; (c, d) Twinning-induced DRX

TB was regarded as a potential nucleation location of recrystallization grains similar to the grain boundary bulging mechanism [23]. During the FSW process, the original TBs were separated from the exact twin/matrix misorientation of 60°⟨111⟩ due to severe plastic deformation, and then they gradually transformed into serrated HAGBs. The dislocation density increased due to the large strain gradient around the serrated TBs. To coordinate the strain, the dislocations near the serrated TBs were rearranged to form LAGBs. As the strain further increased, the LAGBs continuously collected the dislocations and transformed into HAGBs. This twin-dominated nucleation is called twin-induced DRX [24].

It is worth noting that some microstructural features of grain refinement induced by severe plastic deformation were retained in the TMAZ (Fig. 8(f)) because cooling with liquid CO_2 inhibited the recovery of the deformed microstructure. For most FCC metals or alloys with middle or high SFE (such as pure Cu or Al alloys), the increase in dislocation density caused by severe plastic deformation and the segmentation of large grains by the dislocation boundaries are the basic mechanisms for grain refinement, i.e., dislocation subdivision mechanism. In FSW, the materials were deformed at elevated temperatures, and the SFE increased with increasing the deformation temperature [8]. However, the dislocation subdivision mechanism has not yet been reported in the FSW of FCC metals with low SFE. A schematic of the dislocation subdivision in the FSW process is shown in Fig. 10. In the advancing side region, the original grains in the BM began to become involved in the stirring. This can be regarded as the low-strain stage of plastic deformation, in which massive dislocations are formed within the grains. As the materials were driven to the leading side region, the strain increased and dislocation cells were gradually formed. As the strain increased further, the dislocation cells increased, and the cell size decreased as the material reached the retreating side region. The dislocations became concentrated on the cell walls and did not exist within the cell interior. When the diameter of the dislocation reached a minimum size, it no longer decreased with increasing strain. Thereafter, if plastic deformation continued, dislocation cross-slip and dynamic recovery occurred. Eventually, as the material reached the trailing side region, the dislocations on the cell wall continuously tangled

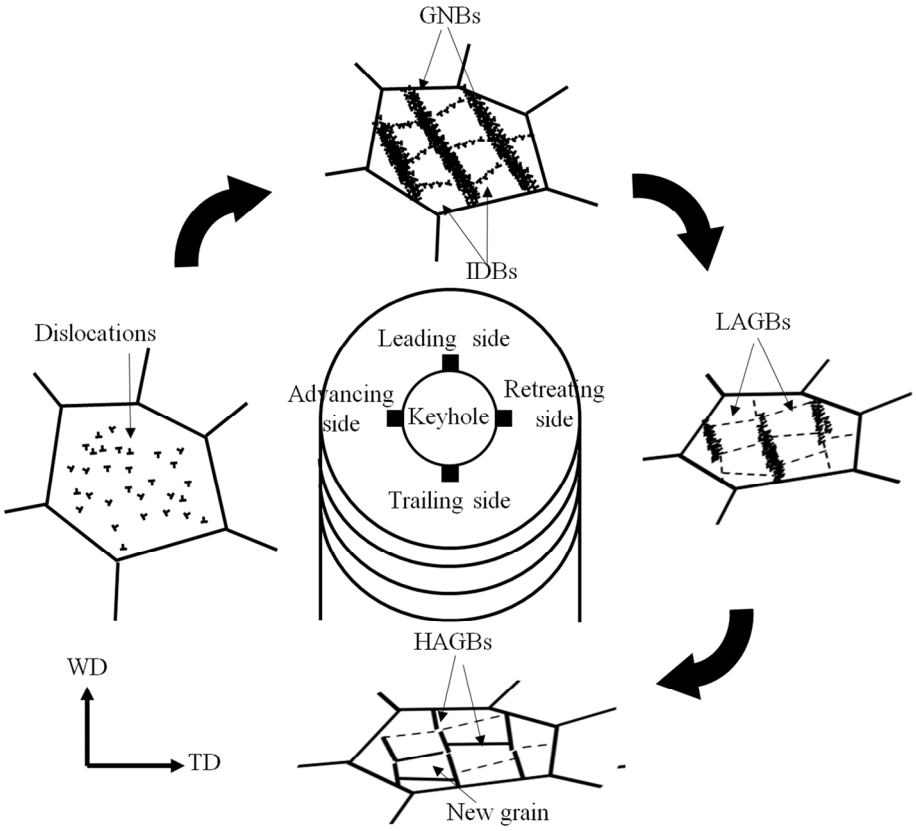

Fig. 10 Schematic diagram of dislocation subdivision mechanism

and a two-dimensional interface was formed such as LAGB or HAGB, resulting in the formation of an ultrafine grain.

To verify dislocation subdivision mechanism on grain refinement during the FSW of α-brass, careful EBSD and TEM characterizations were carried out at the leading side and trailing side regions, and the results are shown in Figs. 11−13. As strain gradually increased in the leading side region, the fraction of LAGBs increased to 68% due to dislocation multiplication in the grains (Figs. 11(a, b)). Dislocation slip occurred to coordinate the strain during plastic deformation, thus forming dislocation boundaries (Fig. 13(a)). These dislocation boundaries, which subdivide the grain into dislocation cells, can be divided into two types: geometrically necessary boundary (GNB) which coordinates the rotation of adjacent regions, and incidental dislocation boundary (IDB) which reduces the system energy [25,26]. Also, initial annealing TBs changed into normal HAGBs (Fig. 11(c)). When the materials reached the trailing side region, the strain reached its maximum value, and ultrafine grain structure was generated (Fig. 12). Dislocations on the GNB and IDB underwent rearrangement and annihilation, which reduced the system energy. Then, dislocation boundaries were transformed into subgrain boundaries. Therefore, the LAGBs ratio decreased to 54%. These subgrain boundaries progressively increased their mis-orientations by absorbing the dislocations and eventually being transformed into HAGBs (Fig. 13(b)).

3.3 Mechanical properties

True stress−strain curves of the SZs are shown in Fig. 14(a), and their tensile properties are summarized in Table 2. Compared with the BM, the total elongation of the SZs was reduced, but their ultimate tensile strength (UTS) and yield strength (YS) were significantly increased. The SZ obtained by RCFSW showed the highest UTS and YS values of 491 MPa and 228 MPa, respectively.

The strain hardening exponent (n) and strain hardening rate (θ) are typically used to evaluate the strain hardening behavior of metal materials [27]. The strain hardening exponent can be calculated with the Hollomon Ludwik equation [28]:

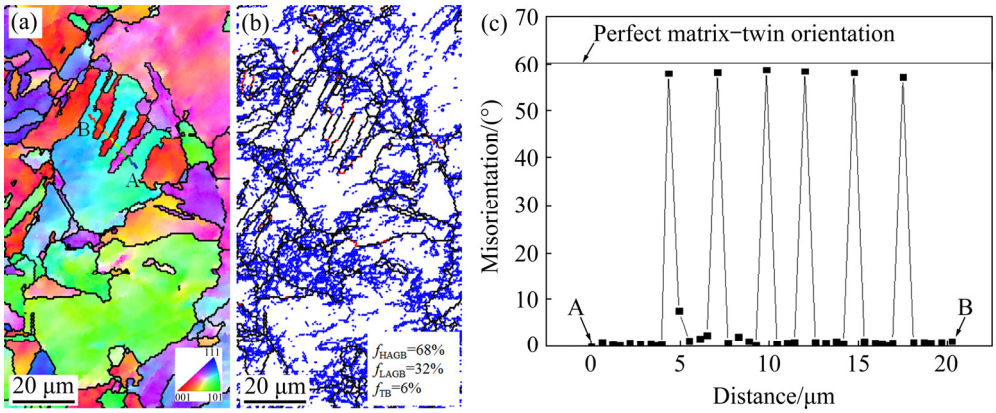

Fig. 11 High-resolution EBSD characterization results of leading side region: (a) Inverse pole figure; (b) Grain boundary map; (c) Point-to-point orientation from A to B shown in (a)

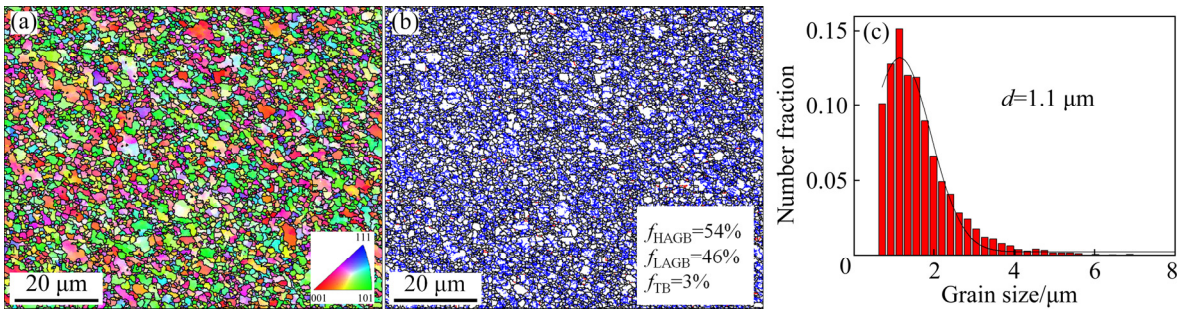

Fig. 12 High-resolution EBSD characterization results of trailing side region: (a) Inverse pole figure; (b) Grain boundary map; (c) Grain size distribution

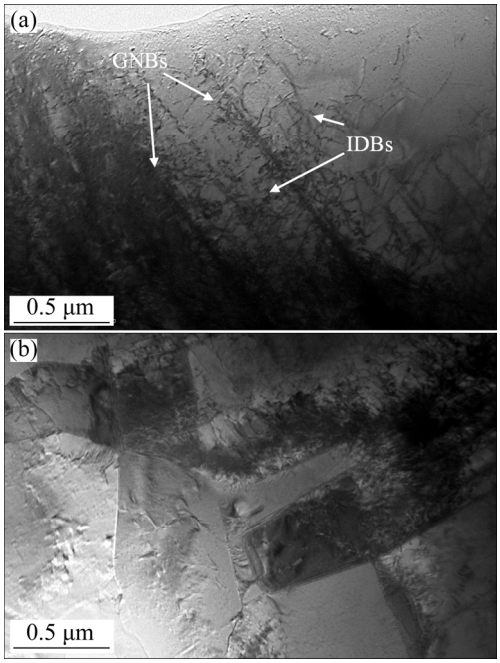

Fig. 13 TEM characteristics of leading side region (a) and trailing side region (b)

$$\sigma=\sigma_y+K(\varepsilon-\varepsilon_y)^n \quad (1)$$

where σ and ε are the true stress and true strain, respectively, σ_y and ε_y are the yield stress and the yield strain of the material, and K is the strength coefficient. By taking the natural logarithm, Eq. (1) can be converted in the following way:

$$\ln(\sigma-\sigma_y)=\ln K+n\ln(\varepsilon-\varepsilon_y) \quad (2)$$

Figure 14(b) shows the fitting results of the strain hardening exponent (n) of the SZs based on Eq. (2). It was found that the n value of the SZ obtained by RCFSW was higher than that obtained by CFSW. Figure 14(c) shows the curves of strain hardening rate versus true strain of the SZs. The two SZs exhibited similar strain hardening stages, namely the initial rapid reduction stage and the subsequent slow reduction stage, which correspond to Stage III and Stage IV of strain hardening behavior, respectively [29].

The YS of the RCFSW increased by 31% compared to that of CFSW, and it was primarily determined by the following three strengthening mechanisms:

$$\sigma_y=\sigma_0+\sqrt{\sigma^2_{\text{Solid-solution}}+\sigma^2_{\text{Grain-boundary}}+\sigma^2_{\text{Dislocation}}} \quad (3)$$

where σ_0 (25 MPa) is the flow stress of pure copper in the annealed state. $\sigma_{\text{Solid-solution}}$, $\sigma_{\text{Grain-boundary}}$, and $\sigma_{\text{Dislocation}}$ are the contributions to the YS of the solution element, grain size, and the dislocation density, respectively.

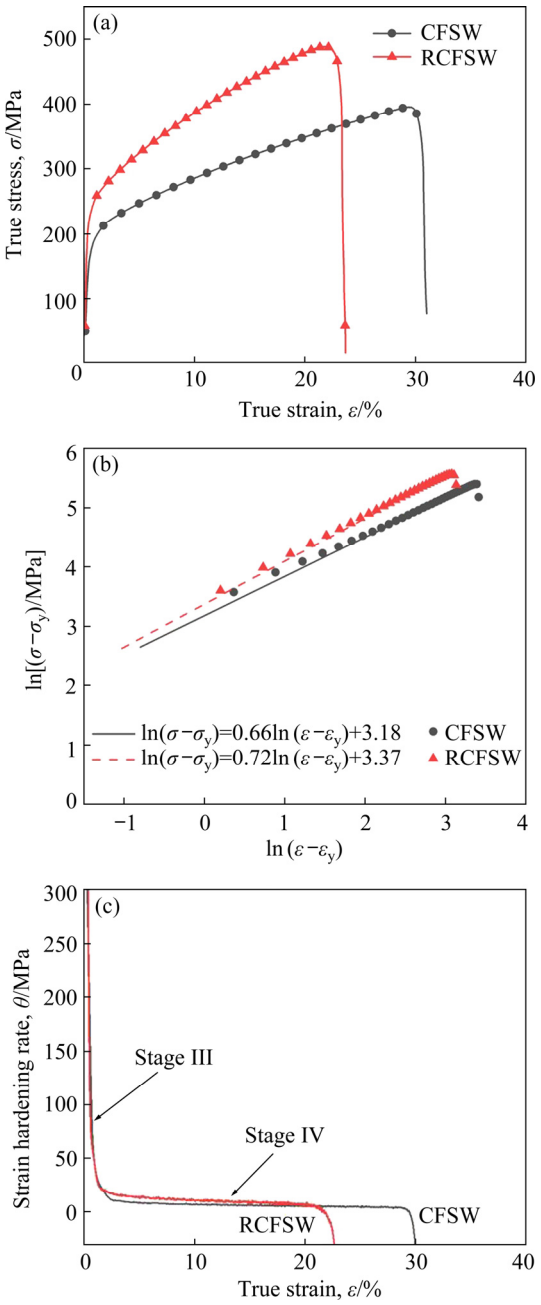

Fig. 14 Tensile test results of SZs obtained by CFSW and RCFSW: (a) True stress−strain curves; (b) Fitting results of strain hardening exponent; (c) Strain hardening rate curves

Table 2 Tensile properties of SZs obtained by CFSW and RCFSW

Process	UTS/MPa	YS/MPa	Total elongation/%
CFSW	397	174	31
RCFSW	491	228	24

(1) Solution strengthening, $\sigma_{\text{Solid-soluiton}}$

The contribution of solid solution element (Zn) to the YS can be calculated as follows [30]:

$$\sigma_{\text{Soli-solution}}=HC^{n} \quad (4)$$

where H (6.16 MPa/wt.%) is the increment of YS of Cu caused by per mass fraction of Zn, C is the content of Zn (wt.%), and n is determined to be 1 for FCC metals. Due to the solid solution of Zn, the lattice distortion in the Cu matrix hinders the dislocation movement. Based on Eq. (4), the contribution of 30% of Zn to the YS is 184.8 MPa.

(2) Grain boundary strengthening, $\sigma_{\text{Grain-boundary}}$

The contribution of grain refinement to the YS can be calculated by Hall−Petch relationship [31,32]:

$$\sigma_{\text{Grain-boundary}}=kd^{-1/2} \quad (5)$$

where k (110 MPa·μm$^{1/2}$) is a constant and d is the average grain size. Based on Eq. (5), the contribution of the grain size to the YS is 36 and 100 MPa for CFSW and RCFSW, respectively. For the SZ in the RCFSW, the increased ratio of HAGB can effectively block the movement of dislocations, so that higher YS can be obtained.

(3) Dislocation strengthening, $\sigma_{\text{Dislocation}}$

The contribution of dislocation density to the YS can be calculated by Taylor relationship [33]:

$$\sigma_{\text{Dislocation}}=M\alpha Gb\sqrt{\rho} \quad (6)$$

where M (3.1) is the Taylor factor, G (39 GPa) is shear modulus, b (0.26 nm) is the magnitude of Burgers vector, α (0.2) is a constant and ρ is dislocation density. Dislocation density is usually evaluated by TEM characterization [34]. The TEM specimen with a thickness of t was tilted to the best position where most dislocation could be observed. Then, a standard square grid was added to the TEM image to calculate the number of intercept points N and the total dislocation length L. Finally, the dislocation density could be estimated using the following formula:

$$\rho=\frac{2N}{Lt} \quad (7)$$

Based on Eq. (7) and Fig. 15, the dislocation densities of CFSW and RCFSW were calculated to be 1.6×10^{15} and 4.8×10^{15} m^{-2}, respectively. By combining Eqs. (6) and (7), the contributions of the dislocations to the YS of CFSW and RCFSW are 25.1 and 43.6 MPa, respectively. As shown in Fig. 5, the ratio of LAGB in the RCFSW was higher than that in the CFSW and mainly composed of substructures, such as dislocation cells [35,36]. This means that the dislocation density in the SZ of the RCFSW was higher than that of the CFSW, which is consistent with the TEM characterization results. Because of the increased cooling rate, both the grain growth and dislocation recovery were restrained, and the dislocations induced by severe plastic deformation were maintained in the grains. The massive dislocation tangles hindered the dislocation propagation and movement. In the next plastic deformation stage, additional stress had to be applied to overcoming the resistance of the dislocation tangles, so the contribution of the dislocation density to the YS of the RCFSW is more obvious.

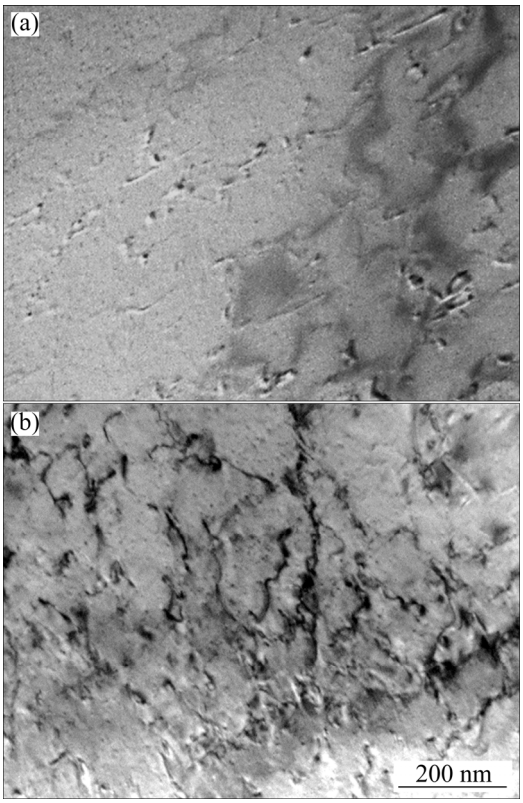

Fig. 15 Dislocation structure in grain interior: (a) CFSW; (b) RCFSW

The experimental and predicted YS values of the SZs are summarized in Table 3. It was found that the experimental and predicted YS of RCFSW were in good agreement, which indicates that the model can accurately predict the YS profile of the RCFSW. For the CFSW, the YS calculated by the same model was 23% higher than the experimental profile because the model did not consider the

Table 3 Contribution of individual strengthening mechanism to YS (MPa)

Process	σ_0	$\sigma_{\text{Solid-solution}}$	$\sigma_{\text{Grain-boundary}}$	$\sigma_{\text{Dislocation}}$	Calculated σ_y	Experimental σ_y
CFSW	25	185	36	25	214	174
RCFSW	25	185	100	43	238	228

unavoidable micropores caused by the Cu and Zn oxides (i.e., stir band), which are usually detected during the CFSW of α-brass (Fig. 16). Due to the existence of micropores, the predicted YS of the CFSW was higher than the experimental value. These investigations into the evolution of the microstructure, mechanical properties, and the strengthening mechanism reveal that remarkable grain refinement and increased dislocation density play key roles in improving the YS of the RCFSW.

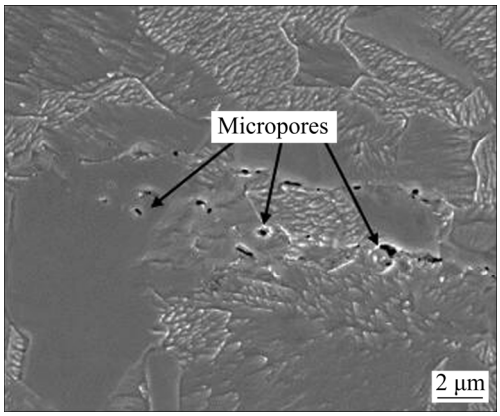

Fig. 16 Micropores formed in SZ of CFSW

The strain hardening behavior after yielding is also closely related to grain size and dislocation density. A high quantity of dislocations and grain boundaries in the RCFSW increased the flow stress for the continued deformation of the material, increasing the strain hardening exponent. As shown in Fig. 14(c), both the SZs in the CFSW and RCFSW exhibited in Stage III and Stage IV of the strain hardening behavior [37]. The strain hardening rate significantly decreased in Stage III. During the dislocation slip process, dislocation annihilation typically occurred, resulting in the reduced strain hardening rate. After a certain amount of strain accumulation, the strain hardening entered into Stage IV. In this stage, the decreasing tendency of the strain hardening rate was slower than it was in Stage III. Due to the dislocation cell continuously absorbing dislocations, the cell structure was transformed into a subgrain boundary when the dislocation density reached a certain value. The strength was improved by substructures, which slowed down the reduction of strain hardening rate. EBSD and TEM results show massive substructures in the grains of RCFSW, giving the weld a relatively high strain hardening rate in Stage IV. More importantly, the total elongation still reached 24%, indicating a relatively good ductility. As shown in Fig. 17, nanoscale deformation twins can be detected in the SZ of RCFSW. Since TB can be regarded as a coherent boundary, it can absorb and decompose dislocations to accommodate the strain caused by plastic deformation [38−40].

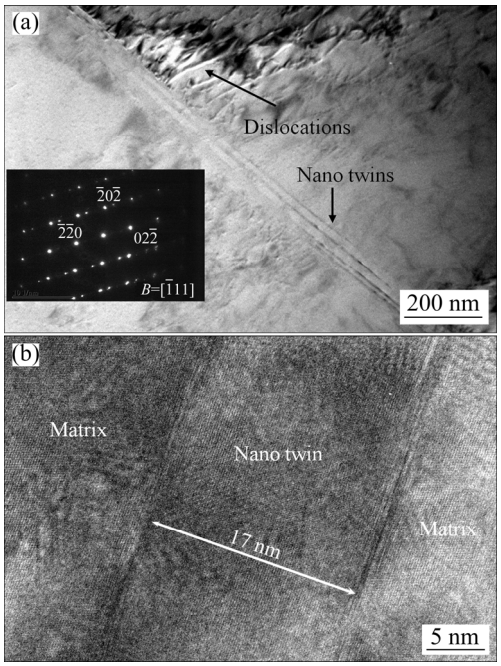

Fig. 17 Nano twins in grain interior of SZ obtained by RCFSW

In summary, the strength and ductility of the SZ obtained by RCFSW can be attributed to the combination of the strengthening mechanisms that include grain boundary strengthening, dislocation strengthening, and twin toughening. The effect of microstructure on the mechanical properties of the SZ obtained by RCFSW is schematically shown in Fig. 18. During FSW, the materials experience severe plastic deformation at high temperatures. Due to liquid CO_2 cooling, the dislocations and

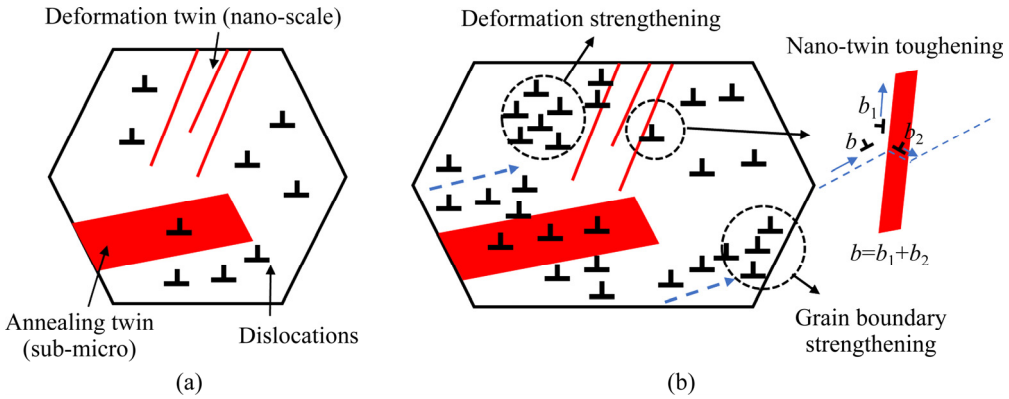

Fig. 18 Schematic diagram of strengthening and toughening mechanism of SZ obtained by RCFSW: (a) Before tension; (b) After tension

nano twins generated during plastic deformation were kept within the grain interior, and the grain growth was restricted. As a result, the RCFSW exhibited ultrafine grains with massive dislocations and TBs. During subsequent tensile test, owing to the heterogeneous structure, the strength of the SZ significantly increased. Furthermore, when a dislocation moved to the TB, it was decomposed into two partial dislocations: one entered in the twin interior, and the other remained at the TB. The TB accommodated considerable plastic strain and effectively released the stress concentration caused by the plastic deformation. As a result, the strength of the RCFSW significantly increased without a considerable decrease in ductility.

4 Conclusions

(1) By using liquid CO_2 cooling, the FSW exhibited an ultrafine grain structure with massive dislocations and nano twins. Heterogeneous microstructures were produced in the α-brass welded with RCFSW technology. Grain refinement in the FSW is attributed to a combination of the mechanisms that include multiple DRX and dislocation subdivision.

(2) Compared with the CFSW, the YS and UTS of the RCFSW were increased by 31% and 24%, respectively, due to the ultrafine grain structure and enhanced dislocation density. The YS of the RCFSW can be accurately predicted by a calculation model due to micropore elimination through liquid CO_2 cooling.

(3) The RCFSW exhibited good strain hardening capacity compared with the CFSW, indicating that the heterogeneous microstructure improved the strain hardening capacity of the SZ.

(4) The total elongation of the RCFSW was 24%. As strength increased, ductility did not decrease because the nano twin boundary could effectively release the stress concentration caused by plastic deformation.

Acknowledgments

The authors are grateful for the financial supports from the Natural Science Foundation of Jiangsu Province, China (No. BK20211067), the National Natural Science Foundation of China (No. 51805145), the Changzhou Science and Technology Program, China (No. CJ20200076), the Fundamental Research Funds for the Central Universities, China (No. B200202229), and the ‘Blue Project’ of Jiangsu Province, China.

References

[1] MOAREF A, RABIEZADEH A. Microstructural evaluation and tribological properties of underwater friction stir processed CP-copper and its alloy [J]. Transactions of Nonferrous Metals Society of China, 2020, 30(4): 972−981.

[2] HWANG Y M, FAN P L, LIN C H. Experimental study on friction stir welding of copper metals [J]. Journal of Materials Processing Technology, 2010, 210: 1667−1672.

[3] WAHID M A, KHAN Z A, SIDDIQUEE A N. Review on underwater friction stir welding: A variant of friction stir welding with great potential of improving joint properties [J]. Transactions of Nonferrous Metals Society of China, 2018, 28(2): 193−219.

[4] HEIDARZADEH A, MIRONOV S, KAIBYSHEV R, ÇAM G, SIMAR A, GERLICH A, KHODABAKHSHI F, MOSTAFAEI A, FIELD D P, ROBSON J D, DESCHAMPS A, WITHERS P J. Friction stir welding/processing of metals

and alloys: A comprehensive review on microstructural evolution [J]. Progress in Materials Science, 2021, 117: 100752.

[5] LIU Xiao-chao, SUN Yu-feng, NAGIRA T, USHIODA K, FUJII H. Effect of stacking fault energy on the grain structure evolution of FCC metals during friction stir welding [J]. Acta Metallurgica Sinica (English Letters), 2020, 33: 1001−1012.

[6] LIU Xiao-chao, ZHEN Yun-qian, SUN Yu-feng, SHEN Zhi-kang, CHEN Hai-yan, GUO Wei, LI Wen-ya. Local inhomogeneity of mechanical properties in stir zone of friction stir welded AA1050 aluminum alloy [J]. Transactions of Nonferrous Metals Society of China, 2020, 30(9): 2369−2380.

[7] LIU Xiao-chao, ZHEN Yun-qian, SHEN Zhi-kang, CHEN Hai-yan, LI Wen-ya, GUO Wei, YUE Zhu-feng. A modified friction stir welding process based on vortex material flow [J]. Chinese Journal of Mechanical Engineering, 2020, 33(1): 1−9.

[8] MERAN C. The joint properties of brass plates by friction stir welding [J]. Materials & Design, 2006, 27(9): 719−726.

[9] MOGHADDAM M S, PARVIZI R, HADDAD-SABZEVAR M, DAVOODI A. Microstructural and mechanical properties of friction stir welded Cu−30Zn brass alloy at various feed speeds: Influence of stir bands [J]. Materials & Design, 2011, 32: 2749−2755.

[10] SUN Y F, FUJII H. Investigation of the welding parameter dependent microstructure and mechanical properties of friction stir welded pure copper [J]. Materials Science and Engineering A, 2010, 527: 6879−6886.

[11] XU Nan, UEJI R, FUJII H. Enhanced mechanical properties of 70/30 brass joint by rapid cooling friction stir welding [J]. Materials Science and Engineering A, 2014, 610: 132−138.

[12] KHODAVERDIZADEH H, MAHMOUDI A, HEIDARZADEH A, NAZARI E. Effect of friction stir welding (FSW) parameters on strain hardening behavior of pure copper joints [J]. Materials & Design, 2012, 35: 330−334.

[13] AFRIN N, CHEN D L, CAO X, JAHAZI M. Strain hardening behavior of a friction stir welded magnesium alloy [J]. Scripta Materialia, 2007, 57: 1004−1007.

[14] LI Sheng-li, YANG Xin-qi, TANG Wen-shen, WANG Fei-xiang, LI Hui-jun. Effect of friction stir processing on microstructure and work hardening behavior of reduced activation ferritic/martensitic steel [J]. Journal of Manufacturing Processes, 2019, 37: 220−231.

[15] XU Nan, UEJI R, FUJII H. Dynamic and static change of grain size and texture of copper during friction stir welding [J]. Journal of Materials Processing Technology, 2016, 232: 90−99.

[16] XU N, CHEN L, FENG R N, SONG Q N, BAO Y F. Recrystallization of Cu−30Zn brass during friction stir welding [J]. Journal of Materials Research and Technology, 2020, 9: 3746−3758.

[17] MIRONOV S, SATO Y S, KOKAWA H. Microstructural evolution during friction stir-processing of pure iron [J]. Acta Materialia, 2008, 56: 2602−2614.

[18] HUANG K, LOGE R E. A review of dynamic recrystallization phenomena in metallic materials [J]. Materials & Design, 2016, 111: 548−574.

[19] XU Nan, SONG Qi-ning, BAO Ye-feng. Investigation on microstructure development and mechanical properties of large-load and low-speed friction stir welded Cu−30Zn brass joint [J]. Materials Science and Engineering A, 2018, 726: 169−178.

[20] SAKAI T, BELYAKOV A, KAIBYSHEV R, MIURA H, JONAS J J. Dynamic and post-dynamic recrystallization under hot, cold and severe plastic deformation conditions [J]. Progress in Materials Science, 2014, 60: 130−207.

[21] SHARMA N K, SHEKHAR S. New insights into the evolution of twin boundaries during recrystallization and grain growth of low-SFE FCC alloys [J]. Materials Characterization, 2020, 159: 110015.

[22] KASSNER M E, BARRABES S R. New developments in geometric dynamic recrystallization [J]. Materials Science and Engineering A, 2005, 410−411: 152−155.

[23] LI Shuo, LUAN Bai-feng, CHU Lin-hua, ZHANG Xin-yu, YUAN Gai-huan, LIU Ri-ping, MURTY K L, LIU Qing. Twinning behaviors and grain refinement mechanisms during friction stir processing of Zr alloy [J]. Materials Characterization, 2020, 163: 110277.

[24] SITDIKOV O, KAIBYSHEV R, SAKAI T. Dynamic recrystallization based on twinning in coarse-grained Mg [J]. Materials Science Forum, 2003, 419−422: 521−526.

[25] HUGHES D A, HANSEN N. The microstructural origin of work hardening stages [J]. Acta Materialia, 2018, 148: 374−383.

[26] HUGHES D A, HANSEN N. High angle boundaries formed by grain subdivision mechanisms [J]. Acta Materialia, 1997, 45: 3871−3996.

[27] LUO Ji, Mei Zhi, TIAN Wen-huai, WANG Zhi-rui. Diminishing of work hardening in electroformed polycrystalline copper with nano-sized and uf-sized twins [J]. Materials Science and Engineering A, 2006, 441: 282−290.

[28] CHEN X H, LU L. Work hardening of ultrafine-grained copper with nanoscale twins [J]. Scripta Materialia, 2007, 57(2): 133−136.

[29] ROLLETT A D, KOCKS U F. A review of the stages of work hardening [J]. Solid State Phenomena, 1993, 35−36: 1−18.

[30] DASHARATH S M, KOCH C C, MULA S. Effect of stacking fault energy on mechanical properties and strengthening mechanisms of brasses processed by cryorolling [J]. Materials Characterization, 2015, 110: 14−24.

[31] LUO P, MCDONALD D T, XU W, PALANISAMY S, DARGUSCH M S, XIA K. A modified Hall–Petch relationship in ultrafine-grained titanium recycled from chips by equal channel angular pressing [J]. Scripta Materialia, 2012, 66: 785−788.

[32] CHEN Ying, GAO Nong, SHA Gang, RINGER S P, STARINK M J. Microstructural evolution, strengthening and thermal stability of an ultrafine-grained Al−Cu−Mg alloy [J]. Acta Materialia, 2016, 109: 202−212.

[33] KUMAR N K, ROY B, DAS J. Effect of twin spacing, dislocation density and crystallite size on the strength of nanostructured α-brass [J]. Journal of Alloys and Compounds, 2015, 618: 139−145.

[34] XUE P, XIAO B L, MA Z Y. High tensile ductility via enhanced strain hardening in ultrafine-grained Cu [J]. Materials Science and Engineering A, 2012, 532: 106−110.
[35] KOCKS U F, MECKING H. Physics and phenomenology of strain hardening: The FCC case [J]. Progress in Materials Science, 2003, 48: 171−273.
[36] MIRONOV S, SATO Y S, KOKAWA H, INOUE H, TSUGE S. Structural response of superaustenitic stainless steel to friction stir welding [J]. Acta Materialia, 2011, 59: 5472−5481.
[37] PANTLEON W. Stage IV work-hardening related to disorientations in dislocation structures [J]. Materials Science and Engineering A, 2004, 387−389: 257−261.
[38] DAO M, LU L, SHEN Y F, SURESH S. Strength, strain-rate sensitivity and ductility of copper with nanoscale twins [J]. Acta Materialia, 2006, 54: 5421−5432.
[39] LU K, LU L, SURESH S. Strengthening materials by engineering coherent internal boundaries at the nanoscale [J]. Science, 2009, 324: 349−352.
[40] XU Nan, ZHANG Wei-da, CAI Si-qi, ZHUO Yue, SONG Qi-ning, BAO Ye-feng. Microstructure and tensile properties of rapid-cooling friction-stir-welded AZ31B Mg alloy along thickness direction [J]. Transactions of Nonferrous Metals Society of China, 2020, 30: 3254−3262.

异质结构改善 α-黄铜快速冷却搅拌摩擦焊缝的强塑性

许 楠，陈 磊，顾帛坤，任紫科，宋亓宁，包晔峰

河海大学 机电工程学院，常州 213022

摘 要：采用传统搅拌摩擦焊(空冷)和快速冷却搅拌摩擦焊(液态二氧化碳)成功焊接 2 mm 厚的 α-黄铜薄板。利用电子背散射衍射和透射电子显微术对焊缝的显微组织和力学性能进行研究。结果表明：传统搅拌摩擦焊缝为均匀等轴晶组织，而快速冷却搅拌摩擦焊缝呈现出含有大量位错和纳米孪晶的异质晶结构。快速冷却搅拌摩擦焊缝的屈服强度和抗拉强度较传统搅拌摩擦焊分别提高 31%和 24%。屈服强度和应变硬化能力的改善归因于晶界强化和位错强化，同时，纳米孪晶可缓解塑性变形引起的应力集中，使焊缝表现出良好的塑性。

关键词：搅拌摩擦焊；黄铜；显微组织；再结晶；力学性能

(Edited by Bing YANG)